




Exploring spin antisymmetrized geminal power Ansätze for strongly correlated spin systems

Zhiyuan Liu ¹, Fei Gao,¹ Guo P. Chen ², Thomas M. Henderson,^{1,2} Jorge Dukelsky,³ and Gustavo E. Scuseria ^{1,2}

¹Department of Physics and Astronomy, Rice University, Houston, Texas 77005-1892, USA

²Department of Chemistry, Rice University, Houston, Texas 77005-1892, USA

³Instituto de Estructura de la Materia, IEM-CSIC, Serrano 123, 28006 Madrid, Spain



(Received 8 March 2023; revised 14 August 2023; accepted 15 August 2023; published xxxxxxxxx)

The antisymmetrized geminal power (AGP), a wave function equivalent to number-projected Hartree-Fock-Bogoliubov (HFB), and number-projected Bardeen-Cooper-Schrieffer (BCS) when working in the paired (natural orbitals) basis, has proven to be an excellent reference for strong pairing interactions. Several correlation methods have also been applied on top of AGP. In this work, we show how AGP can also be applied to spin systems by simply basing its formulation on a spin SU(2) algebra. We here implement spin AGP and spin AGP-based correlation techniques and benchmark them on the XXZ and $J_1 - J_2$ Heisenberg models, both in one and two dimensions. Our results indicate that spin AGP is a promising starting point for modeling spin systems.

DOI: [10.1103/PhysRevB.00.005100](https://doi.org/10.1103/PhysRevB.00.005100)

I. INTRODUCTION

Model spin Hamiltonians provide valuable insight into magnetic materials, high-temperature superconductors, and biochemical processes such as nitrogen fixation [1–3]. They are also important for the study of quantum sensors, cold atoms in optical lattices, and fault-tolerant quantum computers [4–6]. These model Hamiltonians capture diverse physical phenomena without the details of a fully *ab initio* description. Nevertheless, with a few exceptions [7], lattice models of spin systems beyond one dimension are not exactly solvable, and we have to resort to approximate numerical methods.

Here we focus on the ground states of spin lattice models, whose computation is already challenging due to various quantum phases that arise from different interaction strengths [1,8–12]. Particularly, analogous to Hartree-Fock in electronic structure theory, spin-wave functions based on a single spin configuration are inadequate in the strongly correlated regime [13,14]. However, our recent work suggests that methods in electronic-structure theory can be useful for studying spins if they are mapped to fermions without constraints [15].

The antisymmetrized geminal power (AGP) wave function [16,17] has been shown to be a good starting point for certain strongly correlated problems. When correlated with configuration interaction (CI) or coupled cluster (CC) theory [18,19], AGP yields quite accurate results for the reduced Bardeen-Cooper-Schrieffer (BCS) Hamiltonian, which models the kinds of strong correlations seen in conventional superconductors [20,21].

Though AGP was originally developed for paired fermionic systems, the pairing algebra generators satisfy the same SU(2) algebra as spin operators. Inspired by Anderson's resonating valence bond theory, which was applied to study both the Heisenberg model and Hubbard model [22,23], we propose to treat spin systems via AGP. Our results suggest that spin AGP (sAGP) and correlated methods based on it are computationally affordable techniques that can accurately describe the ground states of strongly correlated spin systems.

II. THEORY

A. Antisymmetrized geminal power

The central concept of AGP [16,17] is the geminal, a two-electron wave function created by a geminal creation operator

$$\Gamma^\dagger = \frac{1}{2} \sum_{1 \leq p, q \leq 2M} \eta_{pq} c_p^\dagger c_q^\dagger, \quad (1)$$

where η is antisymmetric, c_p^\dagger is the fermion creation operator for spinorbital p , and indices p, q run over all $2M$ spinorbitals. An AGP state with $2N$ electrons is created by occupying the same geminal N times,

$$|\text{AGP}\rangle = \frac{1}{N!} (\Gamma^\dagger)^N |-\rangle, \quad (2)$$

where $|-\rangle$ is the physical vacuum.

In practice, it is more convenient to work in the natural orbital basis of the geminal, where η is quasisdiagonal [24],

$$\eta = \bigoplus_{p=1}^M \begin{pmatrix} 0 & \eta_p \\ -\eta_p & 0 \end{pmatrix}, \quad (3)$$

displaying a pairing scheme of the spin-orbitals [19]. On this basis, we can write

$$\Gamma^\dagger = \sum_{p=1}^M \eta_p P_p^\dagger, \quad (4)$$

in which we have defined

$$P_p^\dagger = c_p^\dagger c_{\bar{p}}^\dagger \quad (5)$$

and have reindexed the fermion creation operators by p and its paired companion \bar{p} , where p enumerates all M pairs. The AGP then assumes the form of an elementary symmetric polynomial:

$$|\text{AGP}\rangle = \sum_{1 \leq p_1 < \dots < p_N \leq M} \eta_{p_1} \dots \eta_{p_N} P_{p_1}^\dagger \dots P_{p_N}^\dagger |-\rangle. \quad (6)$$

Because AGP is equivalent to number-projected Hartree-Fock-Bogoliubov (HFB) [25] or number-projected BCS in the natural orbital basis, it can be optimized with mean-field cost of $O(M^3)$ [26–28], and its variationally optimized result is guaranteed to be at least as good as Hartree-Fock, which is just a special case of AGP in which only N of the η values are nonzero.

In this paper, we will not worry about the norm of the AGP wave function, which can be normalized by multiplying all the η values by the same constant.

B. AGP for spin systems

The pair creation operator P_p^\dagger and its adjoint P_p , together with the number operator

$$N_p = c_p^\dagger c_p + c_{\bar{p}}^\dagger c_{\bar{p}}, \quad (7)$$

close the the SU(2) commutation algebra:

$$[P_p, P_q^\dagger] = \delta_{pq} (1 - N_p), \quad (8a)$$

$$[N_p, P_q^\dagger] = 2 \delta_{pq} P_p^\dagger. \quad (8b)$$

Following Anderson [29], we can relate the AGP commutation algebra to the spin- $\frac{1}{2}$ SU(2) :

$$[S_p^+, S_q^-] = 2 \delta_{pq} S_p^z, \quad (9a)$$

$$[S_p^z, S_q^+] = \delta_{pq} S_p^+. \quad (9b)$$

Comparing with Eqs. (8), we see that by the bijective mapping

$$S_p^+ \leftrightarrow P_p^\dagger, \quad (10a)$$

$$S_p^- \leftrightarrow P_p, \quad (10b)$$

$$S_p^z \leftrightarrow \frac{N_p - 1}{2}, \quad (10c)$$

we can simply transcribe any expressions for standard AGP matrix elements in the zero seniority [30] fermion space, where all electrons are paired, to those for spin AGP (sAGP for short), and can readily generalize any of the techniques we have introduced for the correlation of AGP to sAGP [18,19,27,31,32]. In the standard pairing AGP case, we have

$$P_p|-\rangle = 0, \quad (11)$$

where $|-\rangle$ denotes the physical vacuum. The corresponding spin vacuum state $|\downarrow\rangle$ is the product state of \downarrow -spins on all sites, and satisfies

$$S_p^-|\downarrow\rangle = 0. \quad (12)$$

The sAGP wave function is thus

$$|\text{sAGP}\rangle = \frac{1}{N!} (\Gamma^\dagger)^N |\downarrow\rangle, \quad (13a)$$

$$\Gamma^\dagger = \sum_p \eta_p S_p^+, \quad (13b)$$

where we have a total of N \uparrow -spins and $(M - N)$ \downarrow -spins, so

$$\langle \text{sAGP} | S^z | \text{sAGP} \rangle = N - \frac{M}{2}. \quad (14)$$

At half filling ($N = M/2$), the sAGP wave function is magnetically neutral.

Incidentally, the inverse mapping of Eqs. (10) has been used to implement quantum computing algorithms for the standard pairing AGP state [33–35].

Let $|p_1 p_2 \cdots p_N\rangle$ be a spin product state (SPS) where the spins are up on sites $p_1, p_2, \cdots p_N$ and down on the others. Equations (13) imply that sAGP is a linear combination of all SPSs in the Hilbert space of the problem, with coefficients

$$\langle p_1 p_2 \cdots p_N | \text{sAGP} \rangle = \eta_{p_1} \eta_{p_2} \cdots \eta_{p_N}. \quad (15)$$

This means that sAGP is a particularly simple matrix product state, whose matrix elements are straightforward and inexpensive to compute [26–28].

We have noted that standard AGP is equivalent to number-projected BCS, which suggests that there should be an equivalent projected mean-field understanding of sAGP. This is indeed the case: sAGP is simply the S^z -projected spin BCS state, where spin BCS (sBCS) is defined as

$$|\text{sBCS}\rangle = \prod_{p=1}^M (1 + \eta_p S_p^+) |\downarrow\rangle, \quad (16)$$

in analogy with the standard BCS given in terms of pairing operators P_p^\dagger and the physical vacuum. When the spin problem is mapped to fermions, spin BCS corresponds to generalized Hartree-Fock (GHF) in which the spin-orbitals break not only S^2 but also S^z symmetry [36–38].

In this paper, in which we specialize to spin Hamiltonians, the GHF wave function has seniority symmetry dictated by the spins, and one could think of sAGP as an S^z -projected general SPS.

III. APPLICATIONS

We benchmark sAGP on two families of spin-lattice systems, the XXZ and $J_1 - J_2$ Heisenberg models [1]. The former captures anisotropic interactions, while the latter includes interactions beyond nearest neighbors.

We focus predominantly on the nearest-neighbor XXZ model. We start with the one-dimensional (1D) case as a prototypical example that illustrates the most important features of sAGP and is exactly solvable via Bethe Ansatz [39]. We then discuss various two-dimensional (2D) XXZ lattices as well as the $J_1 - J_2$ square lattice, which are not integrable, in general.

We first explore sAGP on its own for these systems. While sAGP itself is of modest accuracy, in general, we want to understand its properties to provide context for the correlated sAGP results, which we then compare with conventional correlation methods to show that sAGP is a better starting point for strongly correlated spin systems.

A. Spin AGP for the one-dimensional XXZ model

The XXZ Hamiltonian is

$$H_{\text{XXZ}} = J \sum_{\langle pq \rangle} (S_p^x S_q^x + S_p^y S_q^y + \Delta S_p^z S_q^z) \quad (17a)$$

$$= J \sum_{\langle pq \rangle} \left[\frac{1}{2} (S_p^+ S_q^- + S_p^- S_q^+) + \Delta S_p^z S_q^z \right], \quad (17b)$$

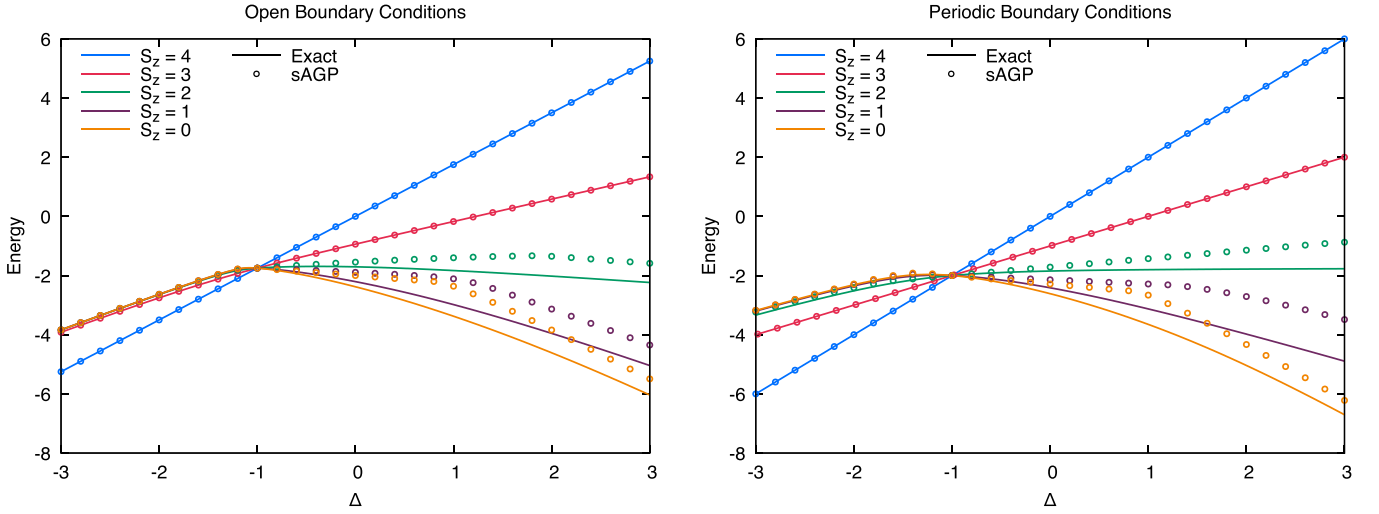


FIG. 1. Energies in the eight-site 1D XXZ Hamiltonian for different S^z sectors and open boundary conditions (left panel) or periodic boundary conditions (right panel). We compare the exact results (lines) against the mean-field optimized sAGP (points). Different colors correspond to different S^z sectors. Spin AGP is very accurate for $\Delta < -1$ and exact for all S^z sectors at $\Delta = -1$. We note that sAGP is always exact for $S^z = 3$ and $S^z = 4$, as explained in Sec. III A 1. The curves for $S^z = 0$ and $S^z = 1$ are hard to distinguish for $\Delta < 0$ in this figure but they are not identical and $S^z = 0$ has a higher energy.

146 where p and q index lattice sites and the notation $\langle pq \rangle$ restricts
 147 the summation over p and q to nearest neighbors. Generally
 148 speaking, we take $J = 1$ in this paper unless otherwise speci-
 149 fied, so the system is antiferromagnetic when $\Delta > 1$.

150 In the 1D case, sites p and q are nearest neighbors
 151 if $|p - q| = 1$. With $J > 0$, it exhibits a Néel antiferro-
 152 magnetic phase for $\Delta \gtrsim 1$ and a ferromagnetic phase for
 153 $\Delta \lesssim -1$. In the interval region $|\Delta| \lesssim 1$, the system is in
 154 the XY phase, characterized by gapless excitations and
 155 long-range correlations [1]. While the ferromagnetic and
 156 antiferromagnetic phases are fairly simple to describe, the
 157 XY phase is much more complicated, and methods based
 158 on a single spin configuration struggle (see below and also
 159 Refs. [13,14]). Spin AGP, however, is exact at $\Delta = -1$,
 160 which gives us hope that it will be able to accurately de-
 161 scribe this challenging phase as Δ progresses from -1
 162 to $+1$.

1. Energies for different S^z sectors

163
 164 Let us start with an overview of the exact and sAGP
 165 ground-state energies for different S^z quantum numbers and
 166 different values of Δ , as shown in Fig. 1. For $\Delta < -1$, the
 167 exact ground state occurs when all the spins are aligned,
 168 i.e., at $S^z = \pm M/2$. For $\Delta > -1$, the exact ground state is
 169 instead $S^z = 0$. At $\Delta = -1$, the different S^z sectors are exactly
 170 degenerate. Spin AGP is exact at $\Delta = -1$ for all S^z sectors
 171 and is highly accurate for $\Delta < -1$. For $\Delta > -1$, sAGP is
 172 exact for $S^z = \pm \frac{M}{2}$ and $S^z = \pm(\frac{M}{2} - 1)$, but shows larger
 173 error as we approach half filling ($S^z = 0$). As a matter of fact,
 174 sAGP is always exact at the $S^z = \pm \frac{M}{2}$ and $S^z = \pm(\frac{M}{2} - 1)$
 175 sectors as it has sufficient variational flexibility. $S^z = \pm \frac{M}{2}$
 176 corresponds to the state where all the spins are aligned
 177 up or down and sAGP naturally capture it by letting $N =$
 178 0 or M , respectively. $S^z = \pm(\frac{M}{2} - 1)$ means the system has
 179 only one \uparrow -spin (or \downarrow -spin) and the exact ground state takes

the form

$$|\Psi\rangle = \sum_p c_p S_p^+ |\downarrow\rangle, \quad (18)$$

which is just the sAGP state with $N = 1$.

2. Bimodal extreme sAGP

182
 183 We now turn to the nature of the sAGP ground state. We
 184 find that η values on adjacent sites have opposite signs for all
 185 values of Δ . When Δ is large and negative, the η values on
 186 the left (or right) half of the lattice are large in magnitude, and
 187 on the other half are small. For a site p , larger $|\eta_p|$ correspond
 188 to larger $\langle S_p^z \rangle$; thus, the fact that the large $|\eta|$ values localize
 189 on the left (or right) side of the lattice means that the \uparrow spins
 190 localize on this side, i.e, we have a two-block ferromagnetic
 191 solution. Due to the breaking of inversion lattice symmetry, \uparrow
 192 spins can either localize on the left half or right, corresponding
 193 to two degenerate states. On the other hand, when Δ is large
 194 and positive, alternating sites exhibit a pattern of large and
 195 small $|\eta|$, corresponding to a Néel arrangement of spins. These
 196 observations are exemplified by the eight-site XXZ chain with
 197 open boundary conditions (OBCs) and $S^z = 0$, whose η values
 198 are depicted in Fig. 2.

199 The more interesting region is of course when $-1 \lesssim \Delta \lesssim$
 200 1 , particularly at $\Delta = -1$, where sAGP is exact. In this region,
 201 the sAGP wave function is what we refer to as a *bimodal*
 202 *extreme*, for which we can choose $\eta = (1, -1, 1, -1, \dots)$,
 203 as can be seen from Fig. 2. An sAGP is extreme when all
 204 η values are the same in magnitude, which corresponds to
 205 each site having equal $\langle S^z \rangle$. We refer to the sAGP as bi-
 206 modal when the η take on two values, in this case, ± 1 .
 207 This bimodal extreme sAGP is the exact ground-state wave
 208 function for $\Delta = -1$ and is the lowest energy sAGP state
 209 throughout this XY phase. Note that extreme AGP also has
 210 a place in the reduced BCS Hamiltonian $H = \sum_p \epsilon_p N_p -$

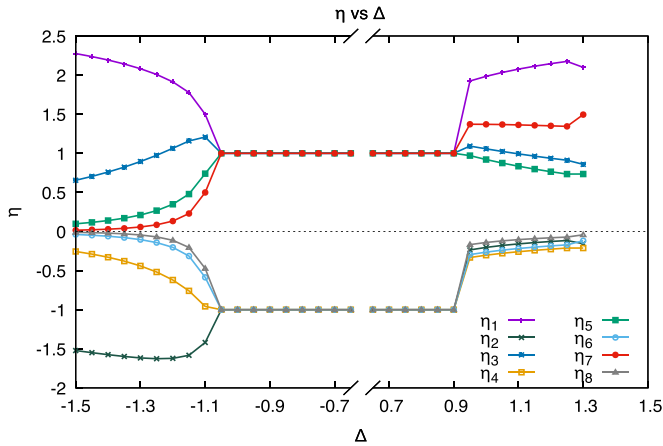


FIG. 2. The sAGP geminal coefficient η as a function of Δ for the eight-site XXZ Heisenberg model with open boundary conditions and $S^z = 0$. For $-1 \leq \Delta \lesssim 1$, the η values are independent of Δ , and $-0.6 < \Delta < 0.6$ has been omitted from the plot. We order the sites from left to right as η_1 to η_8 .

211 $G \sum_{pq} P_p^\dagger P_q$, where, as the interaction strength G goes to
 212 infinity, the values of all η approach the same [18], exhibiting
 213 a unimodal extreme AGP that carries off-diagonal long-
 214 range order, i.e., superconductivity without number-symmetry
 215 breaking [21].

216 We should emphasize again that we do not artificially
 217 choose η to have a bimodal extreme pattern. Instead, we
 218 variationally optimize the η values, and observe that across a
 219 wide range of Δ values, for many different lengths of the XXZ
 220 chain and for many different S^z eigenvalues, and for both pe-
 221 riodic boundary conditions (PBCs) and OBCs, the variational
 222 optimization selects these η values. We also note that bimodal
 223 extreme sAGP is always a stationary point of the energy, and
 224 the points at which the values of η begin to change from
 225 extreme occur when it is no longer the lowest energy solution.

226 Finally, we should say a few words about the physical
 227 meaning of the η values. First, we note that the sign of $\eta_p \eta_q$
 228 determines the sign of $\langle S_p^+ S_q^- + S_p^- S_q^+ \rangle$ [26]. This can also
 229 be seen from Fig. 3. If two sites have oppositely signed η
 230 values, those sites tend to be antiferromagnetically coupled.
 231 The alternating signs of the η values in the bimodal extreme
 232 AGP therefore reflect the Marshall sign rule [40]. The absolute
 233 value of η on a site, as we can see from Eqs. (13), determines
 234 the chance that the spin on that site is flipped to spin up. Sites
 235 with very large or very small relative η values are sites which
 236 are not strongly entangled with the other sites. Sites for which
 237 the absolute values of η are similar are more strongly entan-
 238 gled. The bimodal extreme AGP is actually the maximally
 239 entangled state, and in this case each site has $\langle S^z \rangle = 0$.

3. Approaching the thermodynamic limit

241 Figure 4 shows the energy error per site for the open bound-
 242 ary XXZ chain with different lengths in the $S^z = 0$ sector.
 243 The energy per site in the thermodynamic limit (TDL), e_0 ,
 244 is extrapolated by fitting

$$\frac{E(M)}{M} = e_0 + e_1 \frac{1}{M} + e_2 \frac{1}{M^2} + \dots, \quad (19)$$

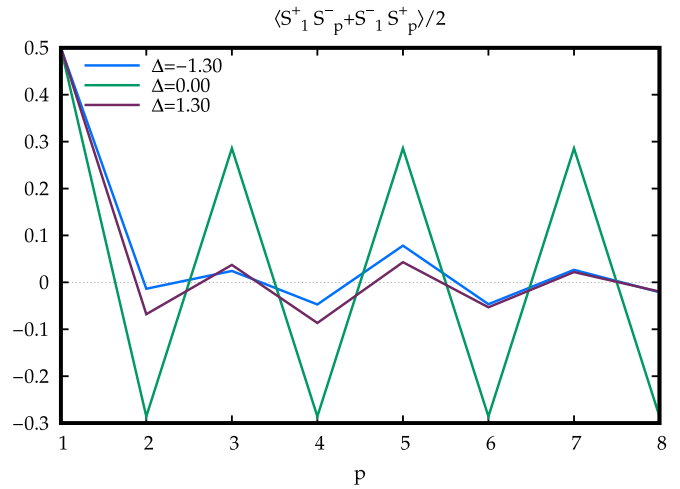


FIG. 3. Correlation function $\langle S_1^+ S_p^- + S_1^- S_p^+ \rangle / 2$ for the eight-site XXZ Heisenberg model with open boundary conditions and $S^z = 0$ for $\Delta = -1.30, 0.00$ and 1.30 , corresponding to the three phases of the XXZ model. We see that $\langle S_1^+ S_p^- + S_1^- S_p^+ \rangle / 2$ have alternating signs for even and odd p , which is a result of the alternating signs of η_p .

245 where we truncate the expansion at second order $e_2 \frac{1}{M^2}$. We
 246 use the same extrapolation scheme for both the sAGP and
 247 the exact energies, and display their differences in the TDL in
 248 Fig. 4. We observe that for all lattice lengths, sAGP reaches its
 249 maximum error around $\Delta = 1$, and the value of Δ at which the
 250 error is the largest grows with the system size. The maximum
 251 sAGP error per site in the TDL is around 0.18. We can also
 252 see that sAGP is quite accurate in the ferromagnetic regime
 253 ($\Delta < -1$) for all system sizes; especially, as the system size
 254 grows, the per-site error reduces.

4. The ferromagnetic XXZ model

255 So far, we have focused on the antiferromagnetic
 256 XXZ model, where $J = 1$. We now briefly discuss the
 257

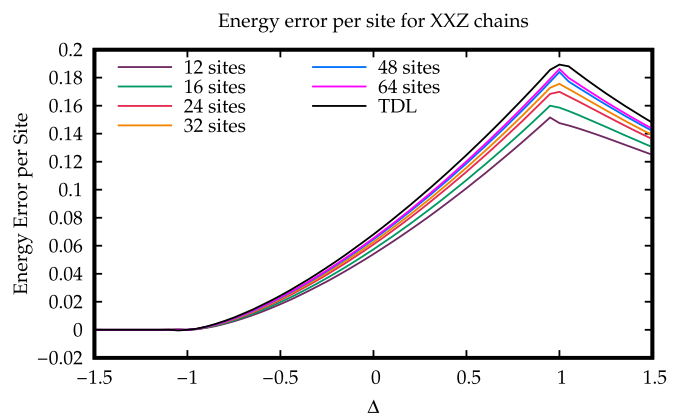


FIG. 4. Energy error per site for 1D XXZ chains with different lengths with open boundary conditions. The thermodynamic limit result is obtained by fitting the sAGP energy result by the inverse of the lattice length. We notice that the per-site energy error grows as system size grows for $\Delta > -1$. It is also noticeable for $\Delta < -1$, the per-site energy error reduces as system size grows.

258 ferromagnetic XXZ model, in which $J = -1$. Because of
 259 the Hamiltonian's overall sign change, the bimodal extreme
 260 sAGP, which is the ground state for the antiferromagnetic
 261 XXZ model at $\Delta = -1$, becomes the highest energy eigen-
 262 state at this point for the ferromagnetic XXZ model. At the
 263 Heisenberg point $\Delta = 1$, an extreme unimodal sAGP where
 264 all the η values are the same becomes the ground state for the
 265 ferromagnetic XXZ model for all S^z sectors with an energy of
 266 $E = -\frac{1}{4}M$ or $E = -\frac{1}{4}(M - 1)$ for PBCs and open boundary
 267 conditions, respectively.

268 B. Spin SU(2) algebras and multimodal extreme sAGPs

269 The bimodal extreme sAGP for antiferromagnetic XXZ
 270 model and the unimodal extreme sAGP for ferromagnetic
 271 XXZ model for the 1D mentioned above are just two special
 272 cases of multimodal extreme sAGPs, all of which can be
 273 formed from collective spin operators which realize a collec-
 274 tive SU(2) algebra,

$$K_k^\pm = \sum_p e^{\pm ikp} S_p^\pm, K^z = \sum_p S_p^z = S^z, \quad (20)$$

275 where k is the lattice momentum. In 1D, $k = \frac{2\pi n}{M}$ with n being
 276 an integer restricted to $-\frac{M}{2} < n \leq \frac{M}{2}$. These three operators
 277 fulfill the SU(2) commutation algebra

$$[K_k^+, K_k^-] = 2K^z, \quad (21a)$$

$$[K^z, K_k^\pm] = \pm K_k^\pm. \quad (21b)$$

278 Note that for momentum $k = 0$, the K -SU(2) algebra reduces
 279 to the spin SU(2) algebra.

280 This K -SU(2) algebra has been recently introduced in the
 281 context of quantum many-body scars in spin lattice systems
 282 [41,42]. However, our goal here is to use it to construct a refer-
 283 ence Ansatz to study many-body correlations in spin-lattice
 284 ground states.

285 The (unnormalized) K -spin extreme sAGP state is a K_k -
 286 spin- $\frac{M}{2}$ multiplet,

$$|N_k\rangle = (K_k^+)^N |\Downarrow\rangle, \quad (22)$$

287 with $K^z = N - \frac{M}{2}$ and $K_k^2 = \frac{M}{2}(\frac{M}{2} + 1)$. Note that each site
 288 has the same $\langle S^z \rangle$ in this wave function. The special cases $k =$
 289 $\frac{2\pi}{m}$ for integer m constitute the m -modal extreme AGP states.
 290 In these cases, we have

$$|N_k\rangle = \left(\sum_p e^{i\frac{2\pi p}{m}} S_p^+ \right)^N |\Downarrow\rangle. \quad (23)$$

291 One can see that the η values are the m th roots of unity. For
 292 $m = 1, 2, 3$, the m -modal extreme AGP states are specifically
 293 called unimodal, bimodal, trimodal extreme AGP, respec-
 294 tively. These m -modal extreme AGP states are a special class
 295 of AGP states, which, as we see here, are the $K_{2\pi/m}$ -spin
 296 eigenstates.

297 We can now ask under what conditions the m -modal
 298 extreme AGP states $|N_k\rangle$ are eigenstates of the XXZ Hamilto-
 299 nian. As demonstrated in Ref. [37], it depends on the geometry
 300 of the lattice. For the 1D XXZ Hamiltonian with PBCs, the

condition is

$$\Delta = \cos(k) = \cos\left(\frac{2\pi n}{M}\right), \quad (24)$$

as shown in Appendix B. In these cases, we have

$$H_{\text{XXZ}}|N_k\rangle = \frac{M}{4}\Delta|N_k\rangle. \quad (25)$$

303 Moreover, the unimodal extreme sAGP is the highest energy
 304 state at the Heisenberg point $\Delta = 1$, and the bimodal extreme
 305 sAGP is the ground state for $\Delta = -1$. The result can also be
 306 extended to OBC. In the interval $-1 < \Delta = \cos(\frac{2\pi n}{M}) < 1$,
 307 the multimodal extreme sAGP are eigenstates of the Hamil-
 308 tonian, known as scarred states, and they describe nonthermal
 309 behavior [43,44].

310 Reduced density matrices of extreme sAGP states are triv-
 311 ial to compute because all elements are identical (ratios of
 312 combinatorial numbers), making it possible to correlate sAGP
 313 with low computational cost.

314 Multimodal extreme sAGPs turn out to be the lowest en-
 315 ergy sAGP states not only for the XY phase ($-1 \lesssim \Delta \lesssim 1$) of
 316 the 1D XXZ model but also for the 2D XXZ and 2D $J_1 - J_2$
 317 models, which will be discussed in Secs. III D and III E. As
 318 with the 1D XXZ model, a multimodal extreme sAGP is the
 319 exact ground state in the 2D XXZ Hamiltonian at a specific
 320 lattice-dependent value of Δ .

321 It should be emphasized that not every sAGP is of extreme
 322 multimodal form; for example, the sAGP ground state in the
 323 1D XXZ model for $|\Delta| \gtrsim 1$ is usually not extreme sAGP.
 324 We observe, however, that for the spin lattice models that
 325 we have studied in this paper, the lowest energy sAGP state
 326 frequently has multimodal extreme character as obtained from
 327 variational optimization.

328 C. Correlating spin AGP in the one-dimensional XXZ model

329 1. Incorporating Jastrow-type correlators

330 After studying the properties of sAGP solutions, we can
 331 now look at improving them by adding correlations. Correlat-
 332 ing AGP with the equivalent of the AGP killing operator
 333 presented in previous work [18],

$$K_{pq} = \eta_p^2 P_p^\dagger P_q + \eta_q^2 P_q^\dagger P_p + \frac{1}{2} \eta_p \eta_q (N_p N_q - N_p - N_q), \quad (26)$$

334 is not helpful here. This is because whenever $\eta_p^2 = \eta_q^2$, as in
 335 the case of a bimodal extreme sAGP state, K_{pq} is Hermitian
 336 and K_{pq}^\dagger also kills sAGP.

337 Fortunately, we can use Hilbert space Jastrow correlators
 338 instead, which generate the same manifold as do the killing
 339 operators in the $\eta_p^2 \neq \eta_q^2$ case [19] because both ultimately
 340 correspond to a geminal replacement theory [31].

341 By Jastrow-type correlators, we mean operators of the form

$$J_2 = \frac{1}{4} \sum_{p < q} \alpha_{pq} N_p N_q \quad (27a)$$

$$\mapsto \sum_{p < q} \alpha_{pq} (2S_p^z - 1)(2S_q^z - 1). \quad (27b)$$

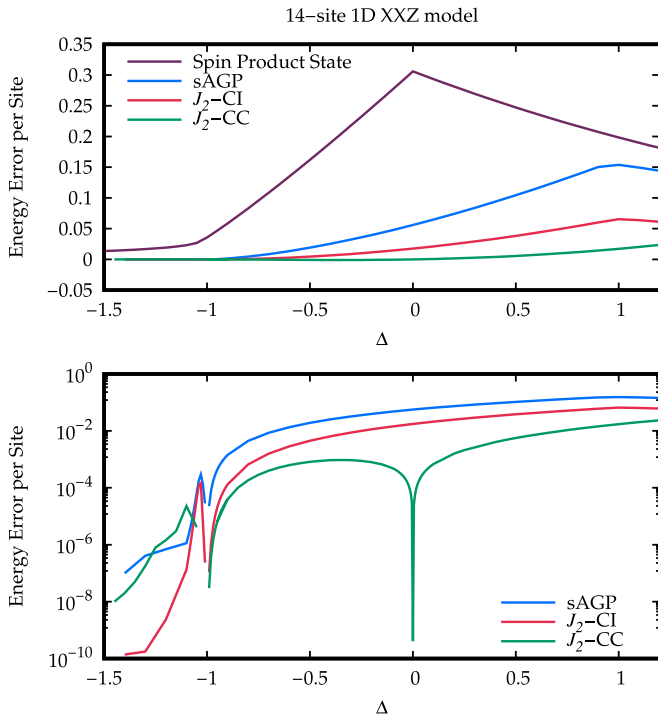


FIG. 5. Energy errors for the 14-site 1D XXZ model with open boundary conditions in the $S^z = 0$ sector, on linear scale (top panel) and logarithmic scale (bottom panel). The J_2 -CI and J_2 -CC methods are based on sAGP. Spin product state results are also included in the top panel for comparison.

342 Since the lower-order Jastrow operator $J_1 = \sum \alpha_p N_p$ al-
 343 ready lurks inside J_2 [32], we can define the J_2 operator for
 344 sAGP as

$$J_2 = \frac{1}{4} \sum_{p < q} \alpha_{pq} S_p^z S_q^z, \quad (28)$$

345 and will use this definition hereafter.

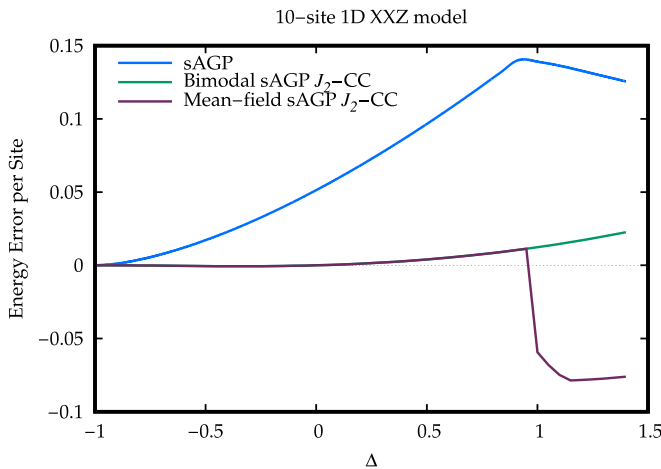


FIG. 6. Errors in the sAGP and J_2 -CC energies based on the mean-field optimized sAGP and the bimodal extreme sAGP in the ten-site XXZ Heisenberg chain with open boundary conditions in the $S^z = 0$ sector.

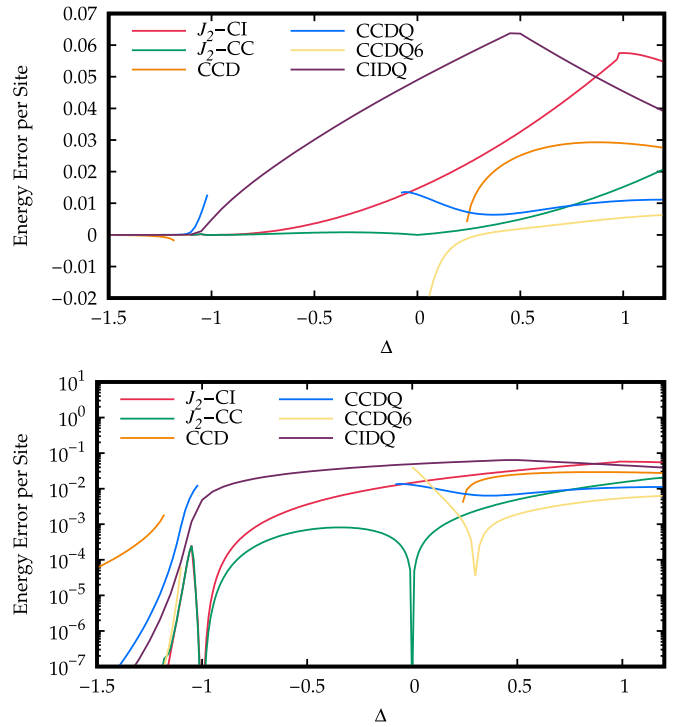


FIG. 7. Energy errors for the 12-site 1D antiferromagnetic XXZ model with open boundary conditions in the $S^z = 0$ sector, on linear scale (top panel) and logarithmic scale (bottom panel). The J_2 -CI and J_2 -CC methods are based on sAGP, while CIDQ, CCD, CCDQ, and CCDQ6 are based on spin product state.

The simplest way to correlate sAGP using these operators
 is by what we refer to as J_2 -CI, which writes

$$|J_2\text{-CI}\rangle = J_2 |s\text{AGP}\rangle, \quad (29)$$

where we generally use the mean-field optimized sAGP as
 a reference. We then evaluate the energy via an expectation
 value and minimize it with respect to the amplitudes α_{pq} .

Somewhat more sophisticated is J_2 -CC, where we use an
 exponential Ansatz instead:

$$|J_2\text{-CC}\rangle = e^{J_2} |s\text{AGP}\rangle. \quad (30)$$

Although intractable in its variational form, a similarity-
 transformed approach is quite feasible [32,45]. The energy
 and residual equations are

$$E_{J_2\text{-CC}} = \langle s\text{AGP} | \bar{H} | s\text{AGP} \rangle, \quad (31a)$$

$$0 = \langle s\text{AGP} | S_p^z S_q^z (\bar{H} - E_{J_2\text{-CC}}) | s\text{AGP} \rangle, \quad (31b)$$

where

$$\bar{H} = e^{-J_2} H e^{J_2}. \quad (32)$$

Although the commutator expansion of \bar{H} does not truncate,
 it can be analytically resummed to yield an expression in terms
 of exponentials of one-body operators J_1 , which act on one
 sAGP state to produce another [32]. Both J_2 -CI and J_2 -CC
 have computational costs proportional to $O(M^4)$ for these
 lattice models.

Figure 5 shows errors of J_2 -CI and J_2 -CC for the 14-site
 antiferromagnetic XXZ model with OBCs. We see that J_2 -CI

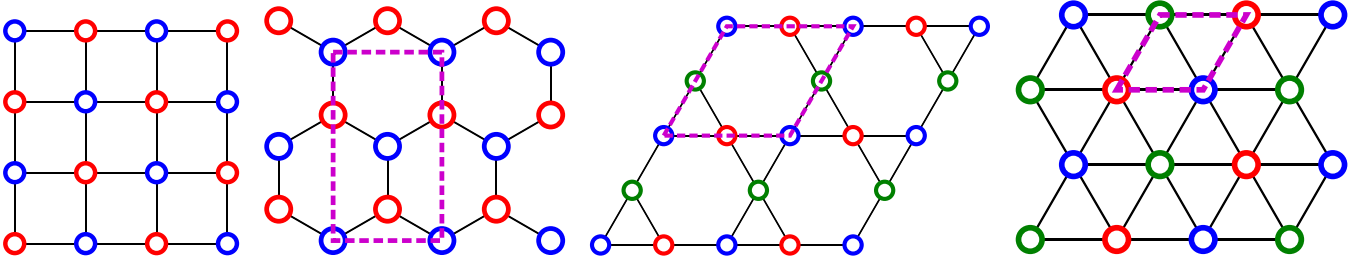


FIG. 8. Assorted 2D lattices. From left to right, these are the square lattice, the honeycomb lattice, the kagome lattice, and the triangular lattice. The purple dashed shape, wherever present, indicates the smallest rectangular cell for the honeycomb lattice and the unit cell for the kagome lattice and triangular lattice. The red, blue, and green open circles indicate the different η values for the sAGP ground state in the XXZ Hamiltonian, which is bimodal extreme for the square and honeycomb lattices, but trimodal extreme for the kagome and triangular lattices.

365 eliminates about half the error of sAGP, while the improve-
 366 ment given by J_2 -CC is significantly larger, with an error one
 367 order of magnitude smaller than the error of sAGP itself. This
 368 is particularly true when J_2 -CC is based on the bimodal ex-
 369 treme sAGP everywhere, and not just where this is the lowest
 370 energy sAGP (Fig. 6). A particularly interesting feature is that
 371 J_2 -CC is exact at $\Delta = 0$. This is true in 1D but not in higher
 372 dimensions. In Appendix A, we prove this exactness for both
 373 OBCs and PBCs.

2. Comparison with conventional correlation methods

To demonstrate the advantage of sAGP-based correlated methods over conventional correlation methods based on SPS, we compare their energies for the 12-site antiferromagnetic XXZ model. Figure 7 shows the energy errors of sAGP-based J_2 -CI and J_2 -CC along with SPS-based configuration interaction doubles and quadruples (CIDQ) and CC doubles to hexuples (CCD, CCDQ, CCDQ6). The two sAGP-based correlated methods have the same computational complexity as SPS-based CIDQ and CCDQ, scaling as $O(M^4)$, while

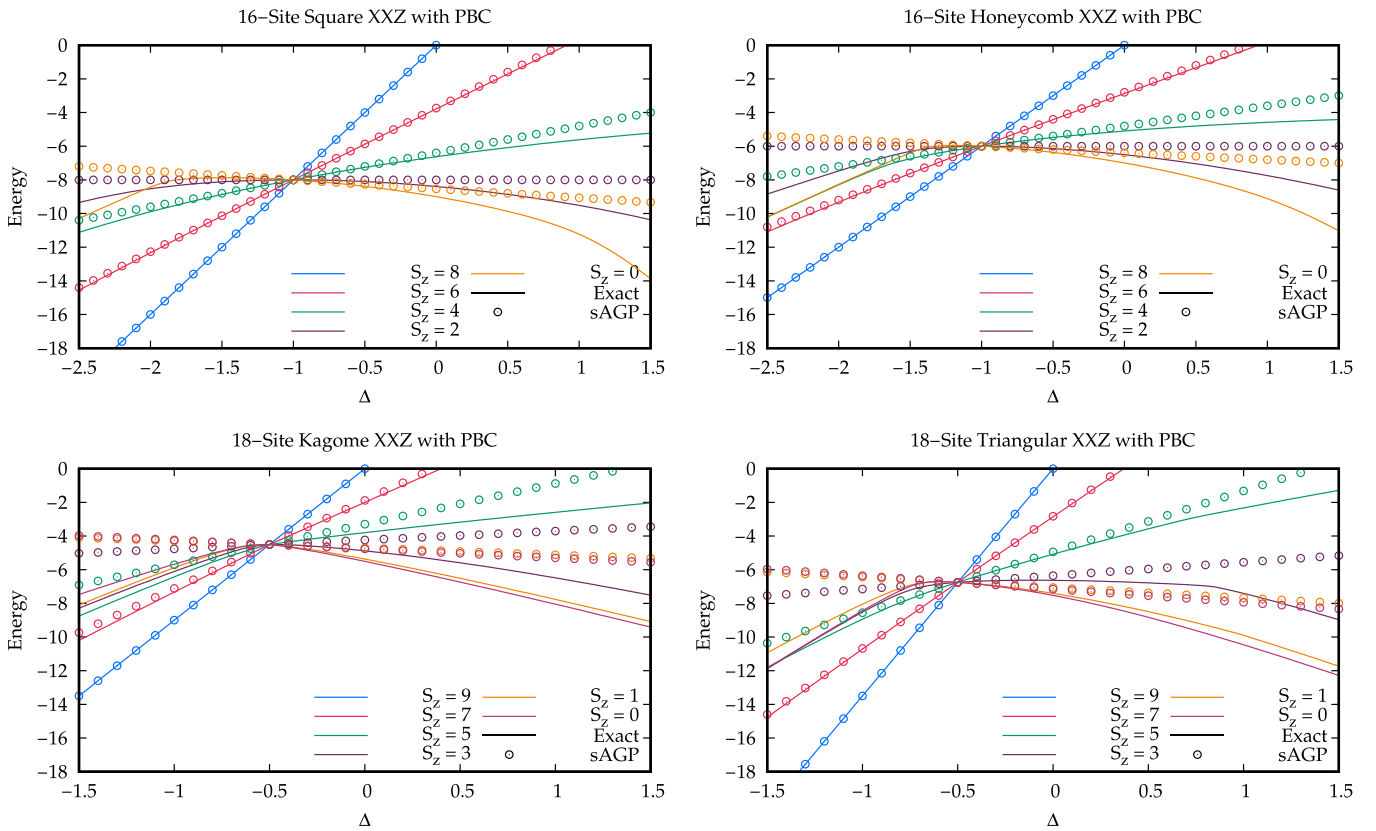


FIG. 9. Multimodal extreme sAGP and exact energies of the XXZ Hamiltonian for different lattices and S^z sectors. The lines correspond to the exact energies and the circles to the multimodal extreme sAGP results. Different colors correspond to different S^z sectors. Top left: Square lattice. Top right: Honeycomb lattice. Bottom left: Kagome lattice. Bottom right: Triangular lattice. All exact and sAGP results have the same energy for all S^z sectors at $\Delta = -1$ (square or honeycomb lattice) or at $\Delta = -1/2$ (kagome or triangular lattice). We note sAGP is always exact for $S^z = \pm \frac{M}{2}$ and $S^z = \pm(\frac{M}{2} - 1)$ (not shown in the figure) for these 2D lattices, for the same reason as in the 1D case discussed in Sec. III A 1.

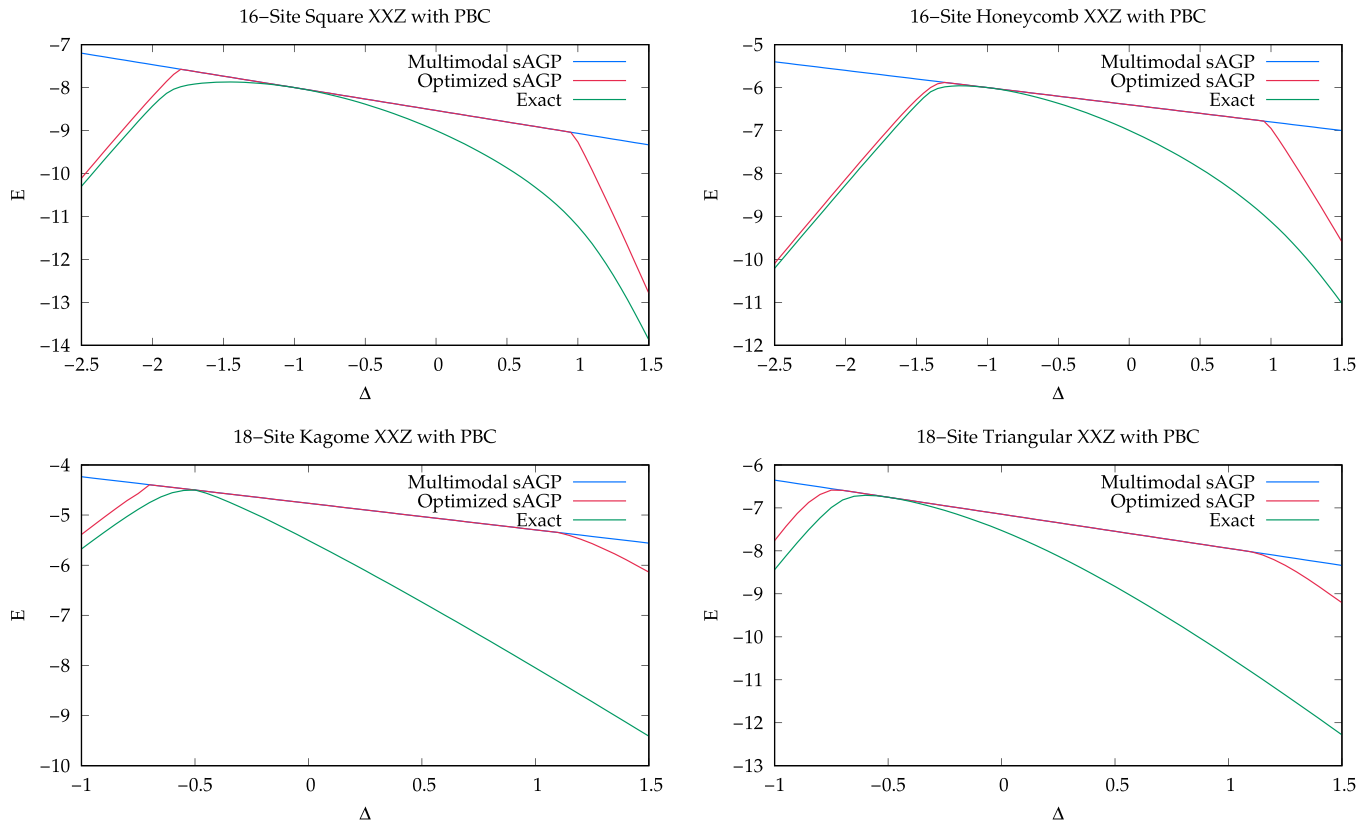


FIG. 10. Exact energies and those of the multimodal extreme sAGP and mean-field optimized sAGP for the XXZ Hamiltonian with $S^z = 0$. Top left: 16-site square lattice. Top right: 16-site honeycomb lattice. Bottom left: 18-site kagome lattice. Bottom right: 18-site triangular lattice.

384 CCD and CCDQ6 scale as $O(M^2)$ and $O(M^6)$, respectively. 409
 385 We note in passing that odd CC excitations (singles, triples, 410
 386 etc.) do not contribute because of S^z symmetry. 411

387 The results of sAGP-based methods are generally superior 412
 388 to those of SPS-based methods with equivalent computational 413
 389 scaling for $\Delta \leq 1$, which corresponds to the ferromagnetic 414
 390 and XY phases. It is important to note that sAGP is exact at 415
 391 $\Delta = -1$, whereas conventional CC calculations break down 416
 392 in this vicinity. As noted above, J_2 -CC is also exact at $\Delta = 0$ 417
 393 and is the most accurate low-scaling correlated method over- 418
 394 all. One may, of course, use an S^z -broken SPS reference to 419
 395 obtain better CC energies [14], but at the cost of breaking 420
 396 physical symmetries of the Hamiltonian, which sAGP and 421
 397 correlated sAGP conserve. 422

398 D. The two-dimensional XXZ model

399 We next test our methods on several XXZ 2D lattices 423
 400 including the square lattice, honeycomb lattice, triangular 424
 401 lattice, and kagome lattice (Fig. 8). In Appendix C, we show 425
 402 analytically that for both PBCs and OBCs with certain bound- 426
 403 ary shapes, the bimodal extreme sAGP is the ground state 427
 404 of the square and honeycomb lattices at $\Delta = -1$, while the 428
 405 trimodal ($m = 3$) extreme sAGP is the ground state of the 429
 406 triangular and kagome lattices at $\Delta = -0.5$. This trimodal 430
 407 extreme sAGP has three distinct η values which we denote by 431
 408 η_1, η_2 , and η_3 . As explained in Sec. III B, these three distinct 432

η values are the three cube roots of 1:

$$\eta_1 = 1, \quad \eta_2 = e^{i\frac{2}{3}\pi}, \quad \eta_3 = e^{i\frac{4}{3}\pi}. \quad (33)$$

410 The arrangements of the η values in different lattices are 411
 412 illustrated in Fig. 8. These analytical results are corroborated 413
 414 by numerical calculations as shown in Fig. 9. The ground 415
 416 states of the 2D XXZ models at these special Δ values have 417
 418 been reported in Ref. [36–38], though they are expressed in a 419
 420 form different from sAGP. 421

422 While we do not wish to dwell on these various lattices in 423
 424 detail, we have a few things to point out. 425

426 First, as we can see in Fig. 10, sAGP is extreme over a 427
 428 range of Δ for all of the lattices. As with the 1D case, the 429
 430 sAGP ground state becomes nonextreme around $\Delta = 1$ for all 431
 432 of the 2D lattices considered here. It also becomes nonextreme 433
 434 for some negative Δ , but the crossover point is lattice depend- 435
 436 ent. We notice that the crossover points for different lattices 437
 438 are correlated with the Δ values at which the extreme sAGP 439
 440 is exact, as discussed above. 441

442 Second, as shown in Fig. 11, J_2 -CC is no longer exact 443
 444 at $\Delta = 0$ for 2D lattices, as opposed to the 1D case. This 445
 446 is reminiscent of Jordan–Wigner transformed Hartree-Fock 447
 448 being exact at $\Delta = 0$ for the 1D spin models but not for 449
 450 their 2D counterparts [15,46]. Although the results of J_2 -CC 451
 452 or J_2 -CI are not as good in 2D as they are in 1D, they still 453
 454 capture more than half the correlation energy missing from the 455
 456 mean-field optimized sAGP methods. They also outperform 457

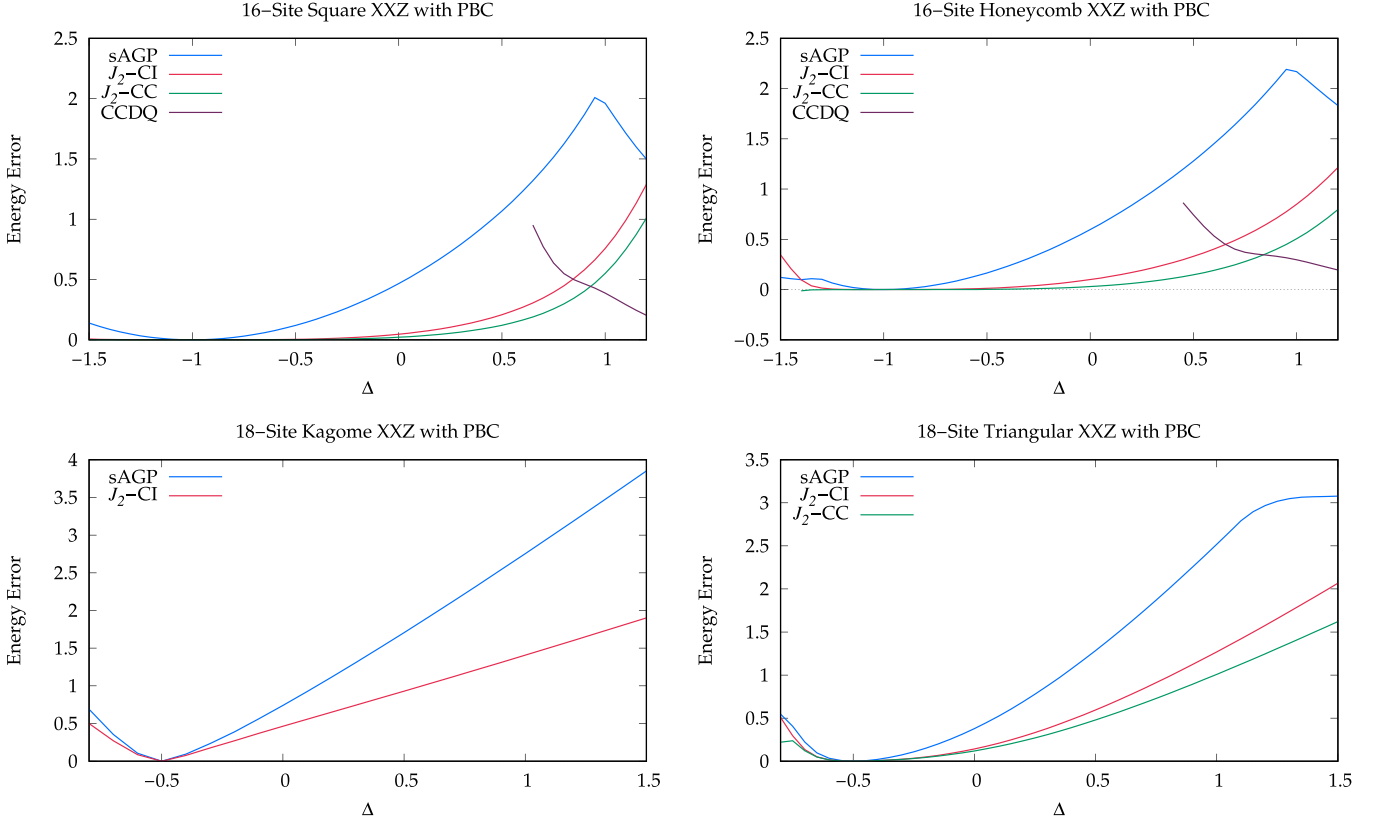


FIG. 11. Energy errors for the mean-field optimized sAGP and for J_2 -CI and J_2 -CC based on the multimodal extreme sAGP, in various XXZ lattices with $S^z = 0$. Top left: 16-site square lattice. Top right: 16-site honeycomb lattice. Bottom left: 18-site kagome lattice. Bottom right: 18-site triangular lattice. Conventional CCDQ results are also shown for the square and honeycomb lattice as a comparison. Note CCDQ fails to converge for square and honeycomb lattice at $\Delta < 0.65$ and $\Delta < 0.45$, respectively. Also note that J_2 -CC does not converge for the kagome lattice and has been omitted from the plot.

434 the conventional SPS-based correlation method (CCDQ here)
 435 for $\Delta < 1$. The error of SPS-based CCDQ grows rapidly as
 436 Δ goes below 1 until it eventually encounters convergence
 437 issues. Conventional CCDQ fails to converge for triangular
 438 and kagome lattices as well. While J_2 -CC also has difficulty
 439 converging for the kagome lattice, it behaves reasonably well
 440 for the triangular lattice.

TABLE I. Energy of the $J_1 - J_2$ model at $J_2 = 1/2$ for different system sizes. We see the energy is only dependent on the system size. For small system sizes, the optimized sAGP is bimodal but nonextreme while, for large system sizes, the bimodal extreme sAGP becomes lower in energy than the nonextreme sAGP.

System size	Extreme	Nonextreme	Energy difference
4×4	-5.0667	-5.2672	0.2005
4×8	-9.0323	-9.2417	0.2094
4×16	-17.0245	-17.2296	0.2050
8×8	-17.0245	-17.2296	0.2050
8×12	-25.1109	-25.2256	0.1146
12×12	-37.4387	-37.2230	-0.2157
16×16	-66.4843	-65.2206	-1.2637

We also test our sAGP-based methods on the 2D square
 $J_1 - J_2$ lattice with PBCs,

$$H_{J_1 - J_2} = J_1 \sum_{\langle pq \rangle} (\vec{S}_p \cdot \vec{S}_q) + J_2 \sum_{\langle\langle pq \rangle\rangle} (\vec{S}_p \cdot \vec{S}_q), \quad (34)$$

where $\langle\langle pq \rangle\rangle$ denotes sites p and q being next-nearest neighbors. We take $J_1 = 1$, and vary J_2 . In TDL, for $J_2 \lesssim 0.45$, the system is in a Néel order where all spins are antiparallel to their nearest neighbors. And for $J_2 \gtrsim 0.61$, the system is in a well-established striped order with spins parallel in the same column (or row) but antiparallel between columns (or rows) [12]. For $J_2 \approx 0.5$, however, the system is in a highly frustrated phase. The ground state is under debate and possible candidates include the plaquette valence-bond state [47], the stripe valence-bond state [48], and gapless spin-liquid state [49].

E. The $J_1 - J_2$ model

We find that the optimized sAGP state for the $J_1 - J_2$ model shows a bimodal pattern over all interaction ranges like the case of XXZ between $-1 < \Delta < 1$ (Fig. 13). For $J_2 < 1/2$, the η values show a Néel pattern, while for $J_2 > 1/2$, η values exhibit a striped pattern. The two patterns are degenerate at $J_2 = 1/2$. As shown in Table I, for small system sizes, the optimized sAGP is bimodal but nonextreme ($|\eta_1| \neq |\eta_2|$),

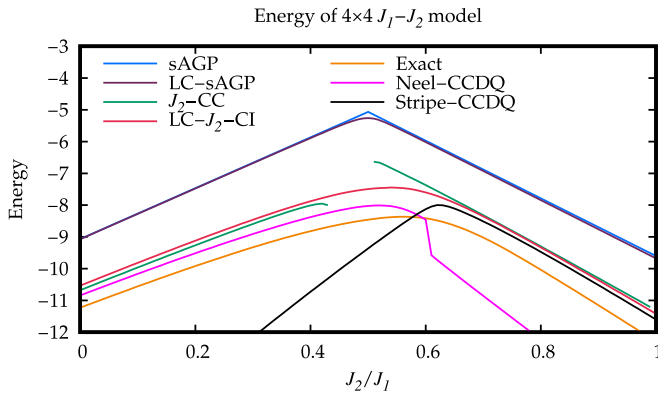


FIG. 12. Energy error for the 4×4 $J_1 - J_2$ model with PBC. LC-sAGP is a linear combination of seven bimodal extreme sAGPs. J_2 -CC and LC- J_2 -CI are correlated methods based on sAGP and LC-sAGP. Néel-CCDQ and stripe-CCDQ are conventional CCDQ results based on different reference states, which are included for comparison with sAGP-based methods.

though the bimodal extreme state ($\eta_1 = 1, \eta_2 = -1$) is still a local minimum. For large system sizes, the bimodal extreme sAGP becomes lower in energy than the nonextreme sAGP.

Figure 12 shows the energies of the bimodal extreme sAGP and its correlated methods for the 4×4 $J_1 - J_2$ model. The two branches of the sAGP curve correspond to the two bimodal extreme patterns (Néel versus striped).

The J_2 -CC [Eq. (30)] energy exhibits a discontinuity at $J_2 = 1/2$ because of the two branches of the reference sAGP. Moreover, for $0.43 < J_2 < 0.5$ (the tail of the left branch in Fig. 12), the J_2 -CC residual equations fail to converge.

To remove the discontinuity and produce well-behaved curves, we consider a reference state that is a linear combination of the relevant sAGPs (LC-sAGP). This is simply an sAGP-based nonorthogonal CI [27]. We find that at least seven bimodal extreme sAGPs are needed if we want to approximate the exact ground state (with additional J_2 -CI-type correlation; vide infra). They include the bimodal extreme sAGP with the Néel pattern and those with the columnwise and row-wise striped patterns, as well as four additional intermediate bimodal extreme sAGP states shown in Fig. 14. These intermediate bimodal extreme sAGPs exhibit a pattern between Néel and striped where each site has only one nearest neighbor that shares its η value.

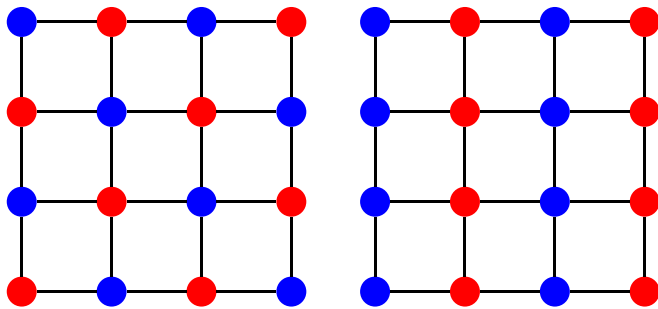


FIG. 13. The sAGP η pattern for the 4×4 $J_1 - J_2$ model with PBC. All sites with the same color have the same η value. The left figure corresponds to $J_2 < 0.5$, and the right $J_2 > 0.5$

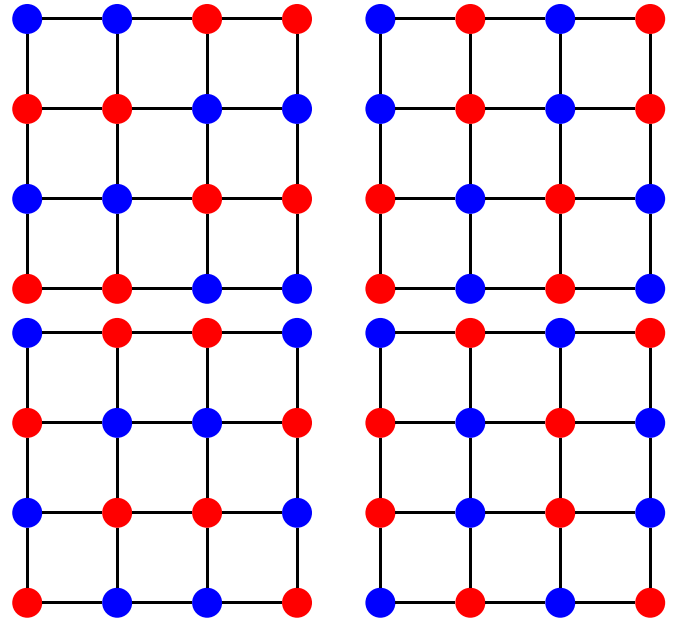


FIG. 14. The four intermediate bimodal extreme sAGP states necessary for LC-sAGP and LC- J_2 -CI for the 4×4 $J_1 - J_2$ model with PBC.

We see that the LC-AGP is well-behaved near $J_2 = 1/2$ but offers little quantitative improvement over a single sAGP elsewhere. In practice, this means that J_2 -CC or J_2 -CI based on this LC-AGP looks a little different from the corresponding methods based on the mean-field optimized sAGP, except for $J_2 \approx 1/2$. Thus, we consider linear combinations of J_2 -CI states as well, shown in Fig. 12 as LC- J_2 -CI. This LC- J_2 -CI is roughly parallel to the exact result, and is comparable to J_2 -CC, but is correctly smooth everywhere.

For comparison, conventional CCDQ was also implemented for the J_1 - J_2 model with the Néel and striped SPS as the reference state, denoted as Néel-CCDQ and stripe-CCDQ, respectively, in Fig. 12. In this case, J_2 -CC and conventional CCDQ are of roughly similar quality. Both behave poorly in the frustrated region $J_2 \approx 1/2$. One great advantage of Jastrow-type correlators over conventional particle-hole-type correlators is that the former, as a similarity transformation, can be solved over any reference state. Future work will explore the use of these J_2 correlators on linear combinations of AGPs which go beyond the simple extreme bimodal AGPs used in Fig. 11.

IV. CONCLUSIONS

In this paper, we have studied sAGP and several sAGP-based correlation methods for the 1D and 2D XXZ models, and the 2D J_1 - J_2 model. With our $O(M^3)$ implementation of mean-field optimized sAGP, we find that optimized sAGP can capture the phase transitions of the XXZ Heisenberg chain and 2D lattices. Furthermore, we show that the optimized sAGP states turn out to be multimodal extreme for the J_1 - J_2 model and the XY phase of the XXZ model, reflecting the translational symmetry of these states. The fact that all η have the same absolute value makes the calculation of correlation

518 methods based on sAGP even easier. These facts suggest
519 that sAGP should be a good reference state for these spin
520 systems.

521 Though correlation methods based on killing operators
522 [18] are not feasible for sAGP, we show that Jastrow operators
523 can serve as good correlators for spin systems. Both J_2 -CI
524 and J_2 -CC yield a significant improvement over mean-field
525 optimized sAGP with reasonable computational cost; J_2 -CC
526 behaves especially well in the XY phase $-1 < \Delta \lesssim 1$ for the
527 XXZ chain and is exact at $\Delta = 0$ in 1D.

528 We have also shown that for the 2D $J_1 - J_2$ model, there
529 are multiple important bimodal extreme sAGP states. The LC-
530 sAGP approach uses a linear combination of these important
531 sAGP states and makes the transition between the Néel pattern
532 and striped pattern smooth. The LC- J_2 -CI energy result on
533 $J_1 - J_2$ model is almost parallel to the exact one.

534 Thus far, we have considered only energies. The behavior
535 of our techniques for correlation functions and other proper-
536 ties will be reported in future work.

537 ACKNOWLEDGMENTS

538 This work was supported by the **U.S. National Science**
539 **Foundation** under Grant No. CHE-2153820. G.E.S. is a
540 **Welch Foundation Chair** (Grant No. C-0036). J.D. acknowl-
541 edges financial support from Projects No. PGC2018-094180-
542 B-I00 and PID2022-136992NB-I00 (MCIU/AEI/FEDER,
543 EU).

544 APPENDIX A: EXACTNESS OF J_2 -CC FOR 1D XXZ 545 AT $\Delta = 0$

546 A general wave function for an M -site 1D spin- $\frac{1}{2}$ system
547 can be written as

$$548 |\psi\rangle = \sum_{1 \leq p_1 < \dots < p_N \leq M} \psi(p_1, \dots, p_N) S_{p_1}^\dagger \dots S_{p_N}^\dagger, \quad (\text{A1})$$

548 where $\psi(p_1, \dots, p_N)$ is the amplitude for the N \uparrow -spins at
549 sites p_1, \dots, p_N .

550 Exact eigenvalues and eigenstates of the 1D XXZ model
551 with PBCs can be found by the Bethe Ansatz, where the
552 ground state amplitude can be written as

$$553 \psi(p_1, \dots, p_N) = \sum_{\sigma \in S_N} A(\sigma) \exp\left(i \sum_{j=1}^N k_{\sigma(j)} p_j\right). \quad (\text{A2})$$

553 The summation runs over all $N!$ permutations of $1, \dots, N$.
554 The amplitudes A relate to the scattering matrix S through

$$555 A(\nu) = S(k_i, k_j) A(\sigma), \quad (\text{A3})$$

555 where the permutation ν is related to the permutation σ by
556 swapping i with j , and

$$557 S(k_i, k_j) = -\frac{e^{i(k_i+k_j)} - 2\Delta e^{ik_j} + 1}{e^{i(k_i+k_j)} - 2\Delta e^{ik_i} + 1}. \quad (\text{A4})$$

557 For the case $\Delta = 0$, $S(k_i, k_j) = -1$, and we can choose
558 $A(\sigma) = (-1)^{\text{sgn}(\sigma)}$. The parameters k_1, \dots, k_n in Eq. (A2) can
559 be solved by the Bethe Ansatz equations:

$$559 e^{ik_i M} = \prod_{j \neq i} S(k_i, k_j). \quad (\text{A5})$$

For even N , the equations reduce to

$$e^{ik_i M} = -1 \quad (\text{A6})$$

and k_i are

$$k_i - \pi = \{\pm\pi/M, \pm 3\pi/M, \pm 5\pi/M \dots\}. \quad (\text{A7})$$

The amplitude $\psi(p_1, \dots, p_N)$ can thus be written as

$$\psi(p_1, \dots, p_N) = \det(C), \quad (\text{A8})$$

563 where the matrix C is defined by $C_{ij} = e^{ik_i p_j}$ and can be
564 recognized as a Vandermonde matrix. Therefore,

$$\det(C) = \prod_{1 \leq i < j \leq N} \sin\left(\frac{\pi}{M}(p_j - p_i)\right) \prod_{l=1}^N e^{i\pi p_l}. \quad (\text{A9})$$

565 According to Eqs. (A8) and (A9), the wave function can be
566 written as J_2 -CC on the bimodal extreme sAGP,

$$|\psi\rangle = e^{J_2} |\text{sAGP}\rangle, \quad (\text{A10})$$

with $\eta_p = e^{i\pi p}$, and J_2 coefficients satisfying

$$\alpha_{pq} = \ln\left(\sin\left(\frac{\pi}{M}(q-p)\right)\right) \quad (\text{A11})$$

for all $1 \leq p < q \leq M$.

568 For OBCs, the derivation is essentially the same, and the
569 ground-state amplitude can still be written as a determinant,
570 but now
571

$$\det(C) = \prod_{1 \leq i < j \leq N} 2 \left(\cos\left(\frac{\pi p_j}{M+1}\right) - \cos\left(\frac{\pi p_i}{M+1}\right) \right) \\ \times \prod_{l=1}^N \sin\left(\frac{\pi p_l}{M+1}\right). \quad (\text{A12})$$

This can be written as J_2 -CC on sAGP with coefficients

$$\eta_p = \sin\left(\frac{\pi p}{M+1}\right), \quad (\text{A13a})$$

$$\alpha_{pq} = \ln\left(2 \left(\cos\left(\frac{\pi q}{M+1}\right) - \cos\left(\frac{\pi p}{M+1}\right) \right)\right). \quad (\text{A13b})$$

572 These η values are not extreme. However, since the J_2
573 operator contains J_1 , and J_1 transforms the η values [32], this
574 means J_2 -CC on bimodal extreme sAGP is also exact.
575

576 APPENDIX B: MULTIMODAL EXTREME SAGP AS THE 577 EIGENSTATE OF 1D XXZ WITH PBC

578 We want to show the multimodal extreme sAGP Eq. (23)
579 generated by the K_k^+ operator Eqn. (20) is an eigenstate of the
580 1D XXZ Hamiltonian with PBC when $\Delta = \cos k$.

581 First we compute the commutators of H_{XXZ} with K_k^+ . Using

$$\left[\sum_{p=1}^M \frac{1}{2} (S_p^+ S_{p+1}^- + S_p^- S_{p+1}^+), K_k^+ \right] \\ = - \sum_{p=1}^M (e^{ik} e^{ikp} S_p^+ S_{p+1}^z + e^{ikp} S_{p+1}^+ S_p^z), \quad (\text{B1a})$$

$$\left[\sum_{p=1}^M S_p^z S_{p+1}^z, K_k^+ \right] = \sum_{p=1}^M (e^{ik} e^{ikp} S_{p+1}^+ S_p^z + e^{ikp} S_p^+ S_{p+1}^z), \quad (\text{B1b})$$

582 we obtain

$$[H_{\text{XXZ}}, K_k^+] = (\Delta - e^{ik}) \sum_{p=1}^M e^{ikp} S_p^+ S_{p+1}^z + (\Delta e^{ik} - 1) \sum_{p=1}^M e^{ikp} S_{p+1}^+ S_p^z, \quad (\text{B2})$$

$$[[H_{\text{XXZ}}, K_k^+], K_k^+] = (\Delta - e^{ik}) e^{ik} \sum_{p=1}^M e^{2ikp} S_p^+ S_{p+1}^+ + (\Delta e^{ik} - 1) \sum_{p=1}^M e^{2ikp} S_{p+1}^+ S_p^+ \quad (\text{B3a})$$

$$= (2\Delta e^{ik} - e^{2ik} - 1) \sum_{p=1}^M e^{2ikp} S_p^+ S_{p+1}^+. \quad (\text{B3b})$$

583 We also have

$$[H_{\text{XXZ}}, K_k^+] |\Downarrow\rangle = -\frac{1}{2} \left((\Delta - e^{ik}) \sum_{p=1}^M e^{ikp} S_p^+ + (\Delta e^{ik} - 1) \sum_{p=1}^M e^{ikp} S_{p+1}^+ \right) |\Downarrow\rangle \quad (\text{B4a})$$

$$= -\frac{1}{2} \left((\Delta - e^{ik}) \sum_{p=1}^M e^{ikp} S_p^+ + (\Delta e^{ik} - 1) e^{-ik} \sum_{p=1}^M e^{ik(p+1)} S_{p+1}^+ \right) |\Downarrow\rangle \quad (\text{B4b})$$

$$= -\frac{1}{2} (2\Delta - e^{ik} - e^{-ik}) \sum_{p=1}^M e^{ikp} S_p^+ |\Downarrow\rangle. \quad (\text{B4c})$$

584 When $\Delta = \cos k$, we have $(2\Delta - e^{ik} - e^{-ik}) = 0$, thus

$$[[H_{\text{XXZ}}, K_k^+], K_k^+] = 0, \quad (\text{B5a})$$

$$[H_{\text{XXZ}}, K_k^+] |\Downarrow\rangle = 0. \quad (\text{B5b})$$

585 Then we can calculate $H_{\text{XXZ}} |N_k\rangle$:

$$H_{\text{XXZ}} |N_k\rangle = H_{\text{XXZ}} (K_k^+)^N |\Downarrow\rangle \quad (\text{B6a})$$

$$= N(K_k^+)^{N-1} [H_{\text{XXZ}}, K_k^+] |\Downarrow\rangle + \frac{N(N-1)}{2} (K_k^+)^{N-2} [[H_{\text{XXZ}}, K_k^+], K_k^+] |\Downarrow\rangle + (K_k^+)^N H_{\text{XXZ}} |\Downarrow\rangle \quad (\text{B6b})$$

$$= \frac{M}{4} \Delta (K_k^+)^N |\Downarrow\rangle \quad (\text{B6c})$$

$$= \frac{M}{4} \Delta |N_k\rangle. \quad (\text{B6d})$$

586 We see that the multimodal extreme sAGP $|N_k\rangle$ becomes
587 an eigenstate of the Hamiltonian H_{XXZ} in 1D, with PBCs.

APPENDIX C: MULTIMODAL EXTREME SAGP AS THE GROUND STATE OF COLORABLE XXZ FOR CERTAIN Δ

590 The proof in the previous Appendix relies on properties of
591 the K_k^+ operator to show that extreme multimodal sAGP is an
592 eigenstate of the 1D XXZ Hamiltonian with PBCs. In fact,
593 as we have noted in the text, multimodal extreme sAGP is

the exact ground state at certain values of Δ even in multiple
594 dimensions. Here, we wish to sketch a proof of this claim. 595

1. Bimodal extreme sAGP for bipartite lattices 596

Bimodal extreme sAGP is the ground state for the 1D XXZ
597 chain and 2D square and honeycomb lattices at $\Delta = -1$. In
598 fact, it is the ground state at this Δ for any lattice so long as
599 the lattice can be colored with only two colors so each pair of
600 neighboring sites has a different color (i.e., for any bipartite
601 lattice). 602

Say p, q are neighboring sites. Let 603

$$H_{pq} = \frac{(S_p^+ S_q^- + S_p^- S_q^+)}{2} + \Delta S_p^z S_q^z. \quad (\text{C1})$$

The XXZ Hamiltonian can then be written as 604

$$H_{\text{XXZ}} = \sum_{\langle pq \rangle} H_{pq}. \quad (\text{C2})$$

We will show that bimodal extreme sAGP is the ground state
605 not only of the whole Hamiltonian H_{XXZ} , but also for each
606 bond H_{pq} . 607

The sAGP is 608

$$|\text{sAGP}\rangle = \frac{1}{N!} \left(\sum_{p=1}^M \eta_p S_p^+ \right) |\Downarrow\rangle \quad (\text{C3a})$$

$$= \sum_{1 \leq p_1 < \dots < p_N \leq M} \eta_{p_1} \dots \eta_{p_N} S_{p_1}^+ \dots S_{p_N}^+ |\Downarrow\rangle. \quad (\text{C3b})$$

609 For a given pair of nearest neighbors p and q , sAGP can be
610 written as

$$\begin{aligned} |sAGP\rangle &= \sum_{\sim} c_{\uparrow\uparrow}(\sim) \eta_p \eta_q |\sim\uparrow_p \uparrow_q \sim\rangle + \sum_{\sim} c_{\downarrow\downarrow}(\sim) |\sim\downarrow_p \downarrow_q \sim\rangle \\ &+ \sum_{\sim} c_{\uparrow\downarrow}(\sim) \eta_p |\sim\uparrow_p \downarrow_q \sim\rangle + \sum_{\sim} c_{\downarrow\uparrow}(\sim) \eta_q |\sim\downarrow_p \uparrow_q \sim\rangle. \end{aligned} \quad (C4)$$

611 Here, \sim represents all possible situations of the sites other
612 than p and q . $c_{\uparrow\uparrow}(\sim), c_{\downarrow\downarrow}(\sim), c_{\uparrow\downarrow}(\sim), c_{\downarrow\uparrow}(\sim)$ are the products
613 of the η values of spin- \uparrow sites in each respective \sim .

614 The two summations for $|\sim\downarrow_p \uparrow_q \sim\rangle$ and $|\sim\uparrow_p \downarrow_q \sim\rangle$ are the
615 same, as there are $M - 2$ other sites, $N - 1$ of which have \uparrow
616 spin. For the same reason, $c_{\downarrow\uparrow}(\sim) = c_{\uparrow\downarrow}(\sim)$, so

$$\begin{aligned} |sAGP\rangle &= \sum_{\sim} c_{\uparrow\uparrow}(\sim) \eta_p \eta_q |\sim\uparrow_p \uparrow_q \sim\rangle + \sum_{\sim} c_{\downarrow\downarrow}(\sim) |\sim\downarrow_p \downarrow_q \sim\rangle \\ &+ \sum_{\sim} c_{\uparrow\downarrow}(\sim) (\eta_p |\sim\uparrow_p \downarrow_q \sim\rangle + \eta_q |\sim\downarrow_p \uparrow_q \sim\rangle). \end{aligned} \quad (C5)$$

617 For bimodal extreme sAGP, $\eta_p = -\eta_q$, so

$$\begin{aligned} |sAGP\rangle &= - \sum_{\sim} c_{\uparrow\uparrow}(\sim) |\sim\uparrow_p \uparrow_q \sim\rangle + \sum_{\sim} c_{\downarrow\downarrow}(\sim) |\sim\downarrow_p \downarrow_q \sim\rangle \\ &+ \sum_{\sim} c_{\uparrow\downarrow}(\sim) \eta_p (|\sim\uparrow_p \downarrow_q \sim\rangle - |\sim\downarrow_p \uparrow_q \sim\rangle). \end{aligned} \quad (C6)$$

618 Now note that

$$H_{pq} |\sim\uparrow_p \uparrow_q \sim\rangle = \Delta S_p^z S_q^z |\sim\uparrow_p \uparrow_q \sim\rangle = \frac{\Delta}{4} |\sim\uparrow_p \uparrow_q \sim\rangle, \quad (C7)$$

$$H_{pq} |\sim\downarrow_p \downarrow_q \sim\rangle = \Delta S_p^z S_q^z |\sim\downarrow_p \downarrow_q \sim\rangle = \frac{\Delta}{4} |\sim\downarrow_p \downarrow_q \sim\rangle, \quad (C8)$$

$$(C9)$$

$$H_{pq} (|\sim\uparrow_p \downarrow_q \sim\rangle - |\sim\downarrow_p \uparrow_q \sim\rangle) \quad (C10a)$$

$$= \left(\frac{(S_p^+ S_q^- + S_p^- S_q^+)}{2} + \Delta S_p^z S_q^z \right) (|\sim\uparrow_p \downarrow_q \sim\rangle - |\sim\downarrow_p \uparrow_q \sim\rangle) \quad (C10b)$$

$$= \left(-\frac{1}{2} - \frac{1}{4} \Delta \right) (|\sim\uparrow_p \downarrow_q \sim\rangle - |\sim\downarrow_p \uparrow_q \sim\rangle). \quad (C10c)$$

3 619 When $\Delta = -1$, we obtain

$$H_{pq} |sAGP\rangle = -\frac{1}{4} |sAGP\rangle. \quad (C11)$$

620 This shows that the bimodal extreme sAGP is an eigenstate of
621 every bond H_{pq} in the lattice at $\Delta = -1$.

622 Now we will show it is the ground state at this Δ . Recall
623 the Hamiltonian of the single bond, given in Eq. (C1). For

any states of the entire lattice, only the spin configurations at
624 site p and q have an influence on the single bond, so we can
625 safely project the state to the subspace that only contains these
626 two sites and diagonalize the Hamiltonian of the bond in this
627 subspace. The eigenvalues are $-\frac{1}{4}, -\frac{1}{4}, -\frac{1}{4}, \frac{1}{4}$. The bimodal
628 extreme sAGP energy of $-\frac{1}{4}$ means that it is a ground state
629 for this single bond. Thus bimodal extreme sAGP is a ground
630 state for all bonds in the lattice at $\Delta = -1$. This means it is
631 also a ground state of the entire Hamiltonian and
632

$$H_{XXZ} |sAGP\rangle = -\frac{\text{Number of bonds}}{4} |sAGP\rangle. \quad (C12)$$

Note that this result relies only on the form of the Hamiltonian
633 and on the lattice being bipartite. In particular, it is true for any
634 number of dimensions, for any boundary conditions, and for
635 any (integer) S^z sector.
636

2. Trimodal extreme sAGP for tripartite lattices

637 The kagome and triangular lattices cannot be colored with
638 only two colors due to the triangular shape (Fig. 8). These
639 lattices are three-colorable (i.e., tripartite). We will show that
640 trimodal extreme sAGP is an eigenstate of the triangular
641 shapes in the three-colorable lattices.
642

643 Say p, q, r are three sites that form a triangle. In trimodal
644 extreme sAGP, η_p, η_q, η_r are correspondingly $1, e^{\pm \frac{2i\pi}{3}}$. Let

$$H_{\Delta} = H_{pq} + H_{qr} + H_{rp}. \quad (C13)$$

645 The trimodal extreme sAGP, when focusing on these three
646 sites, is

$$\begin{aligned} |sAGP\rangle &= \sum_{\sim} c_{\uparrow\uparrow\uparrow}(\sim) \eta_p \eta_q \eta_r |\sim\uparrow_p \uparrow_q \uparrow_r \sim\rangle \\ &+ \sum_{\sim} c_{\uparrow\uparrow\downarrow}(\sim) (\eta_p \eta_q |\sim\uparrow_p \uparrow_q \downarrow_r \sim\rangle \\ &+ \eta_p \eta_r |\sim\uparrow_p \downarrow_q \uparrow_r \sim\rangle + \eta_r \eta_q |\sim\downarrow_p \uparrow_q \uparrow_r \sim\rangle) \\ &+ \sum_{\sim} c_{\uparrow\downarrow\downarrow}(\sim) (\eta_p |\sim\uparrow_p \downarrow_q \downarrow_r \sim\rangle + \eta_q |\sim\downarrow_p \uparrow_q \downarrow_r \sim\rangle \\ &+ \eta_r |\sim\downarrow_p \downarrow_q \uparrow_r \sim\rangle) \\ &+ \sum_{\sim} c_{\downarrow\downarrow\downarrow}(\sim) |\sim\downarrow_p \downarrow_q \downarrow_r \sim\rangle. \end{aligned} \quad (C14)$$

647 Following a similar procedure as we have outlined for the
648 two-colorable case, it can be shown that

$$H_{\Delta} |sAGP\rangle = -\frac{3}{8} |sAGP\rangle. \quad (C15)$$

649 Thus the trimodal extreme sAGP is the ground of state of
650 a triangle that contains the three different η values. In PBCs,
651 both kagome and triangular lattices are composed purely of
652 such triangles and trimodal extreme sAGP is the exact ground
653 state at $\Delta = -0.5$. For OBCs, trimodal extreme sAGP is the
654 exact ground state at $\Delta = -0.5$ only when the lattice breaks
655 none of these triangles.

[1] U. Schollwöck, J. Richter, D. J. Farnell, and R. F. Bishop, *Quantum Magnetism* (Springer, 2008), Vol. 645.

[2] Z.-H. Cui, H. Zhai, X. Zhang, and G. K.-L. Chan, *Science* **377**, 1192 (2022).

- [3] L. Noodleman, C. Peng, D. Case, and J.-M. Mouesca, *Coord. Chem. Rev.* **144**, 199 (1995).
- [4] E. J. Davis, B. Ye, F. Machado, S. A. Meynell, W. Wu, T. Mittiga, W. Schenken, M. Joos, B. Kobrin, Y. Lyu *et al.*, *Nat. Phys.* **19**, 836 (2023).
- [5] J. J. García-Ripoll, M. A. Martín-Delgado, and J. I. Cirac, *Phys. Rev. Lett.* **93**, 250405 (2004).
- [6] C. Broholm, R. J. Cava, S. A. Kivelson, D. G. Nocera, M. R. Norman, and T. Senthil, *Science* **367**, eaay0668 (2020).
- [7] A. Kitaev, *Ann. Phys.* **321**, 2 (2006).
- [8] S. Yan, D. A. Huse, and S. R. White, *Science* **332**, 1173 (2011).
- [9] S. R. White and A. L. Chernyshev, *Phys. Rev. Lett.* **99**, 127004 (2007).
- [10] D. Sellmann, X.-F. Zhang, and S. Eggert, *Phys. Rev. B* **91**, 081104(R) (2015).
- [11] Z. Zhu and S. R. White, *Phys. Rev. B* **92**, 041105(R) (2015).
- [12] W.-Y. Liu, S.-S. Gong, Y.-B. Li, D. Poilblanc, W.-Q. Chen, and Z.-C. Gu, *Sci. Bull.* **67**, 1034 (2022).
- [13] R. F. Bishop, J. B. Parkinson, and Y. Xian, *Phys. Rev. B* **46**, 880 (1992).
- [14] R. F. Bishop, D. J. Farnell, and J. B. Parkinson, *J. Phys.: Condens. Matter* **8**, 11153 (1996).
- [15] T. M. Henderson, G. P. Chen, and G. E. Scuseria, *J. Chem. Phys.* **157**, 194114 (2022).
- [16] A. J. Coleman, *J. Math. Phys.* **6**, 1425 (1965).
- [17] P. Ring and P. Schuck, *The Nuclear Many-Body Problem* (Springer Science & Business Media, 2004).
- [18] T. M. Henderson and G. E. Scuseria, *J. Chem. Phys.* **151**, 051101 (2019).
- [19] T. M. Henderson and G. E. Scuseria, *J. Chem. Phys.* **153**, 084111 (2020).
- [20] J. Bardeen, L. N. Cooper, and J. R. Schrieffer, *Phys. Rev.* **108**, 1175 (1957).
- [21] C. N. Yang, *Rev. Mod. Phys.* **34**, 694 (1962).
- [22] P. W. Anderson, *Mater. Res. Bull.* **8**, 153 (1973).
- [23] P. W. Anderson, G. Baskaran, Z. Zou, and T. Hsu, *Phys. Rev. Lett.* **58**, 2790 (1987).
- [24] L.-K. Hua, *Am. J. Math.* **66**, 470 (1944).
- [25] G. E. Scuseria, C. A. Jiménez-Hoyos, T. M. Henderson, K. Samanta, and J. K. Ellis, *J. Chem. Phys.* **135**, 124108 (2011).
- [26] A. Khamoshi, T. M. Henderson, and G. E. Scuseria, *J. Chem. Phys.* **151**, 184103 (2019).
- [27] R. Dutta, G. P. Chen, T. M. Henderson, and G. E. Scuseria, *J. Chem. Phys.* **154**, 114112 (2021).
- [28] G. P. Chen and G. E. Scuseria, *J. Chem. Phys.* **158**, 231102 (2023).
- [29] P. W. Anderson, *Phys. Rev.* **112**, 1900 (1958).
- [30] L. Bytautas, T. M. Henderson, C. A. Jiménez-Hoyos, J. K. Ellis, and G. E. Scuseria, *J. Chem. Phys.* **135**, 044119 (2011).
- [31] R. Dutta, T. M. Henderson, and G. E. Scuseria, *J. Chem. Theory Comput.* **16**, 6358 (2020).
- [32] A. Khamoshi, G. P. Chen, T. M. Henderson, and G. E. Scuseria, *J. Chem. Phys.* **154**, 074113 (2021).
- [33] A. Khamoshi, F. A. Evangelista, and G. E. Scuseria, *Quantum Sci. Technol.* **6**, 014004 (2021).
- [34] A. Khamoshi, G. P. Chen, F. A. Evangelista, and G. E. Scuseria, *Quantum Sci. Technol.* **8**, 015006 (2023).
- [35] A. Khamoshi, R. Dutta, and G. E. Scuseria, *J. Phys. Chem. A* **127**, 4005 (2023).
- [36] H. J. Changlani, D. Kochkov, K. Kumar, B. K. Clark, and E. Fradkin, *Phys. Rev. Lett.* **120**, 117202 (2018).
- [37] S. Pal, P. Sharma, H. J. Changlani, and S. Pujari, *Phys. Rev. B* **103**, 144414 (2021).
- [38] E. Chertkov and B. K. Clark, *Phys. Rev. B* **104**, 104410 (2021).
- [39] C. N. Yang and C. P. Yang, *Phys. Rev.* **150**, 321 (1966).
- [40] W. Marshall, *Proc. R. Soc. London A* **232**, 48 (1955).
- [41] N. O’Dea, F. Burnell, A. Chandran, and V. Khemani, *Phys. Rev. Res.* **2**, 043305 (2020).
- [42] J. Ren, C. Liang, and C. Fang, *Phys. Rev. Res.* **4**, 013155 (2022).
- [43] N. Regnault, S. Moudgalya, and B. A. Bernevig, *Rep. Prog. Phys.* (2022).
- [44] R. Melendrez, B. Mukherjee, P. Sharma, A. Pal, and H. J. Changlani, *arXiv:2212.13790*.
- [45] J. M. Wahlen-Strothman, C. A. Jiménez-Hoyos, T. M. Henderson, and G. E. Scuseria, *Phys. Rev. B* **91**, 041114(R) (2015).
- [46] H. Nishimori and G. Ortiz, *Elements of Phase Transitions and Critical Phenomena* (OUP, Oxford, 2010), p. 220.
- [47] M. E. Zhitomirsky and K. Ueda, *Phys. Rev. B* **54**, 9007 (1996).
- [48] S. Sachdev and R. N. Bhatt, *Phys. Rev. B* **41**, 9323 (1990).
- [49] L. Capriotti, F. Becca, A. Parola, and S. Sorella, *Phys. Rev. Lett.* **87**, 097201 (2001).